Obstructions in the lower airways lead to altered airflow patterns in the central airway

Daniel S. Hariprasad[a,b], Bora Sul[a,b], Chang Liu[c], Kenneth T. Kiger[c], Talissa Altes[d], Kai Ruppert[e], Jaques Reifman[a,*], Anders Wallqvist[a]

[a] Department of Defense Biotechnology High Performance Computing Software Applications Institute, Telemedicine and Advanced Technology Research Center, United States Army Medical Research and Development Command, FCMR-TT, 504 Scott St., Fort Detrick, MD 21702, USA
[b] The Henry M. Jackson Foundation for the Advancement of Military Medicine, Inc., 6720A Rockledge Dr., Bethesda, MD 20817, USA
[c] Department of Mechanical Engineering, University of Maryland, Glenn L. Martin Hall, 4298 Campus Dr., College Park, MD 20742, USA
[d] Department of Radiology, University of Missouri, University Hospital, One Hospital Dr., Columbia, MO 65212, USA
[e] Department of Radiology, University of Pennsylvania, 3400 Spruce St., Philadelphia, PA 19104, USA

ARTICLE INFO

ABSTRACT

A characteristic feature of obstructive lung diseases is the narrowing of small airways, which affects regional airflow patterns within the lung. However, the extent to which these patterns differ between healthy and diseased states is unknown. To investigate airflow patterns in detail, we first used particle image velocimetry measurements to validate a large eddy simulation model of flow in a patient-specific geometry. We then predicted flow patterns in the central airway under exhalation for three flow conditions—normal, intermediate, and severe—where boundary conditions represented the effect of lower airway obstructions. We computed Pearson correlation coefficients (R) to assess the similarity of flow patterns, and found that flow patterns demonstrated the greatest differentiation between flow conditions in the right main bronchi ($R \leq 0.60$), whereas those in the secondary branches and regions of the trachea showed high correlation ($R \geq 0.90$). These results indicate that although flow patterns are distinct between flow conditions, the choice of measurement location is critical for differentiation.

1. Introduction

Obstructive lung diseases, such as asthma and chronic obstructive pulmonary disease (COPD), typically result in narrowing, or obstruction, of small airways in the lung, *i.e.*, those with a diameter of less than 2 mm (Hogg et al., 1968; Kuyper et al., 2003; McDonough et al., 2011; Van den Berge et al., 2011). The obstructions increase resistance to flow in the small airways and are non-uniformly distributed throughout the lung (Turato et al., 2001; Burgel, 2011; Berg and Wright, 2016). This results in regional variations in lung function, including ventilation heterogeneity (Downie et al., 2007; Tzeng et al., 2009). However, the effect of obstructions on regional flow characteristics within the lung is not well understood.

Multi-detector computed tomography (CT) creates high-resolution images of the lung that are used to investigate disease characteristics in a wide array of pulmonary diseases, including asthma (Walker et al., 2012; Ash and Diaz, 2017), COPD (Diaz et al., 2010; Haruna et al., 2010; McDonough et al., 2011), and pulmonary fibrosis (Gotway et al., 2007; Kitaguchi et al., 2010). However, while CT produces a highly detailed view of lung structures, it does not provide information about flow characteristics within the lung. In contrast, the pulmonary function test measures volumetric flow in the lung and provides information about certain flow characteristics, such as bulk flow rate (Ruppel and Enright, 2012). Nevertheless, this test cannot discern any regional heterogeneities underlying the flow.

Computational fluid dynamics (CFD) models are useful for investigating flow characteristics in the lung and assisting in the design of clinical treatments. Idealized lung geometries have been used widely in previous CFD studies, in particular, the Weibel Type A model (Weibel et al., 1963). For example, Yang et al. (2006) examined the alteration to flow characteristics during inhalation in a lung geometry based on the three-dimensional (3-D), 23 generation Weibel lung model. Their study, which used a series of four-generation truncations of the lung, demonstrated that obstructions significantly influence airflows both up- and down-stream through the presence of recirculation regions. Moreover, they determined that obstructions significantly increase flow

---

resistance. In addition, Sul et al. (2014) studied the alteration to airflow characteristics resulting from obstructions in a Weibel model of the 8th–14th generations of the lung. They computed Pearson correlation coefficients to compare airflow pattern similarity and found that the patterns were clearly different for high-rate expiratory flows but not for inspiratory flows.

Advances in CT imaging techniques and software have led to the increased use of patient-specific geometries in CFD models. For instance, Choi et al. (2009) studied intrasubject variability of airflow characteristics and determined that two morphological features of the lung were primarily responsible for the variation in flows between subjects. Separately, Xi et al. (2014) compared exhaled aerosol patterns (also called aerosol fingerprints) between healthy and diseased subjects and found a correlation between the exhaled patterns and lung condition. In another study, Qi et al. (2018) examined the flow characteristics of subjects with tracheal bronchus and showed that compared to healthy subjects, the structural features of this condition presented individualized flow attributes.

Whereas the use of patient-specific geometries is widely accepted, the use of patient-specific boundary conditions remains a potential concern in CFD models, because frequently used boundary conditions (*i.e.*, uniform pressure or velocity) fail to reproduce physiologically realistic distributions of airflow within the lungs. Previously, De Backer et al. (2010) and Yin et al. (2010) independently proposed physiologically derived boundary conditions and found them to be in good agreement with *in vivo* CT measurements. In addition, Yin et al. (2010) found that the use of improper boundary conditions produce errors in flow characteristics, indicating the necessity of using patient-specific boundary conditions to accurately represent flow characteristics in the lung.

In a separate study, Sul et al. (2018) assessed flow characteristics under exhalation in an idealized geometry with patient-specific boundary conditions that represented regional changes in flow distribution due to a pulmonary disease, which they termed lobar flow fractions. Their results demonstrated that flow patterns differ throughout the central airway because of changes in flow distribution. However, that study relied on an idealized lung geometry. Patient-specific geometries, which are considerably more complex than idealized ones, lead to much more complex flow behavior (Lin et al., 2007; Choi et al., 2009; Bernate et al., 2017). This increase in flow complexity is likely to affect the observed flow patterns in the central airway and may alter the degree of pattern similarity compared to that observed in the idealized geometry.

In this study, we extended the analysis of Sul et al. (2018) to include a patient-specific geometry and investigated flow pattern differences due to changes in lobar flow fractions representing lower airway obstructions. To this end, we validated a CFD model with particle image velocimetry (PIV) measurements, predicted flow patterns for three flow conditions under exhalation, and then used Pearson correlation coefficients and root-mean-square differences to determine their similarity.

2. Methods

2.1. Geometry and flow conditions

Fig. 1a shows the patient-specific central airway geometry based on the reconstruction and modification of a CT scan provided by the University of Virginia (Charlottesville, VA). The scan, obtained from a healthy, 39-year-old female subject, comprised the oral cavity, oropharynx, larynx, trachea, and bronchial tree extending up to the sixth generation. We processed the CT scan with MIMICS (Materialise, Ann Arbor, MI) and created a 3-D model. We further modified the 3-D model to make it suitable for construction of an *in vitro* model with 3-Matic (Materialise, Ann Arbor, MI), by increasing the cross-sectional area of the glottis and enlarging the model by a scale factor of 1.8. Although we enlarged the geometry for the *in vitro* model, some of the distal bronchi
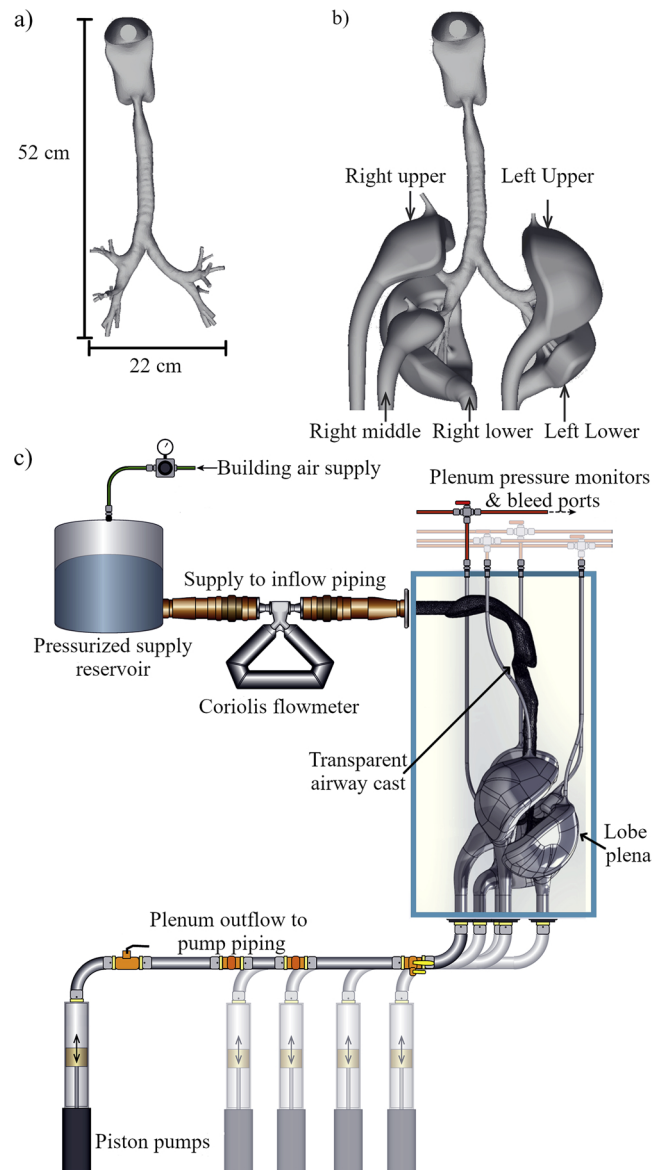

Fig. 1. Model geometry and experimental setup. a) Frontal view of the patient-specific central airway obtained from a computed tomography scan of a healthy, 39-year-old female subject, comprised of the oral cavity, oropharynx, larynx, trachea, and bronchial tree extending up to the sixth generation. b) Geometry of the full model with lobe plena attached to the distal bronchi of the central airway, where each plenum is attached to the bronchi corresponding to a single lung lobe. c) Schematic of the particle image velocimetry experimental setup with individual piston pumps attached to each lobe plenum in a transparent cast of the full model geometry. With this setup, the flow rate for each lobe plenum is independently controlled.

were too small in diameter to be sufficiently resolved by the 3-D printing technique we adopted for this study (described below in Section 2.2). Because of this limitation, we reduced the total number of distal bronchi from 42 to 26 so that the diameters were greater than 0.3 cm and could be fully resolved by 3-D printing. The resulting model had a tracheal diameter of 3 cm, with the diameters of the distal bronchi varying between 0.3 and 0.9 cm. Fig. 1b shows the full model geometry with lobe plena attached to the distal bronchi of the central airway. Each lobe plenum represented the lower airways of a lung lobe. We attached the lobe plena accordingly to the central airway; that is, we grouped the distal bronchi by lung lobe and attached the bronchi to the corresponding lobe plenum. Each lobe plenum terminated in a single inlet, enabling us to control the flow rates for the five lobe plena

Table 1
Flow conditions and their associated lobar flow fractions.

Flow condition	Lobar flow fraction (%)				
	Left upper lobe	Left lower lobe	Right upper lobe	Right middle lobe	Right lower lobe
Normal	21.0	28.0	14.0	7.0	30.0
Intermediate	24.5	22.5	22.0	9.0	22.0
Severe	28.0	17.0	30.0	11.0	14.0

independently.

For this study, we considered a steady exhalation flow condition with a total flow rate Q of 770.4 mL/s (this correlates to a flow rate of 600 mL/s on the human scale). We chose this flow rate as it corresponds to a mean breathing flow rate during moderate activity (Anderson et al., 2006), which falls within the physiological range of human breathing. We specified the fraction of the total flow rate distributed to each lobe plenum, which we termed the lobar flow fraction. Table 1 shows the three flow conditions considered (normal, intermediate, and severe) where each corresponds to a different set of lobar flow fractions. We derived the lobar flow fractions for two of the flow conditions (normal and severe) from two subjects at the University of Virginia following a previously described protocol (Yin et al., 2010; Sul et al., 2018), corresponding to a healthy subject and a subject diagnosed with COPD,

respectively. We determined the lobar flow fractions for each subject by calculating the volume change of each lung lobe from peak inspiration to peak expiration, and calculated the volume change of each lobe relative to the total volume change of the lungs. For the normal condition, we derived lobar flow fractions from the subject that was the basis for the central airway geometry. For the severe condition, we evaluated lobar flow fractions for three subjects with COPD and found them to show similar patterns of distribution. In all cases, the lower lobes exhibited lower flow fractions compared to the healthy subject, along with concomitant increases in flow fractions for the upper lung lobes—*e.g.*, the lobar flow fraction for the left lower lobe is 28% in the healthy subject and 17% in the COPD subject, while the fraction for the left upper lobe is 21% in the healthy subject and 28% in the COPD subject. Comparing the three subjects, the difference between flow fractions for a given lung lobe was at most 10% of the total flow. Subsequently, we chose one representative subject for the severe condition whose flow fractions represented the median of those evaluated. To represent a subject in the early stages of disease progression, we determined the intermediate flow condition by averaging the lobar flow fractions from the normal and severe conditions.

2.2. Experimental methods

Fig. 1c shows a schematic diagram of the flow model used for the PIV experiments. We used fused deposition modeling techniques to
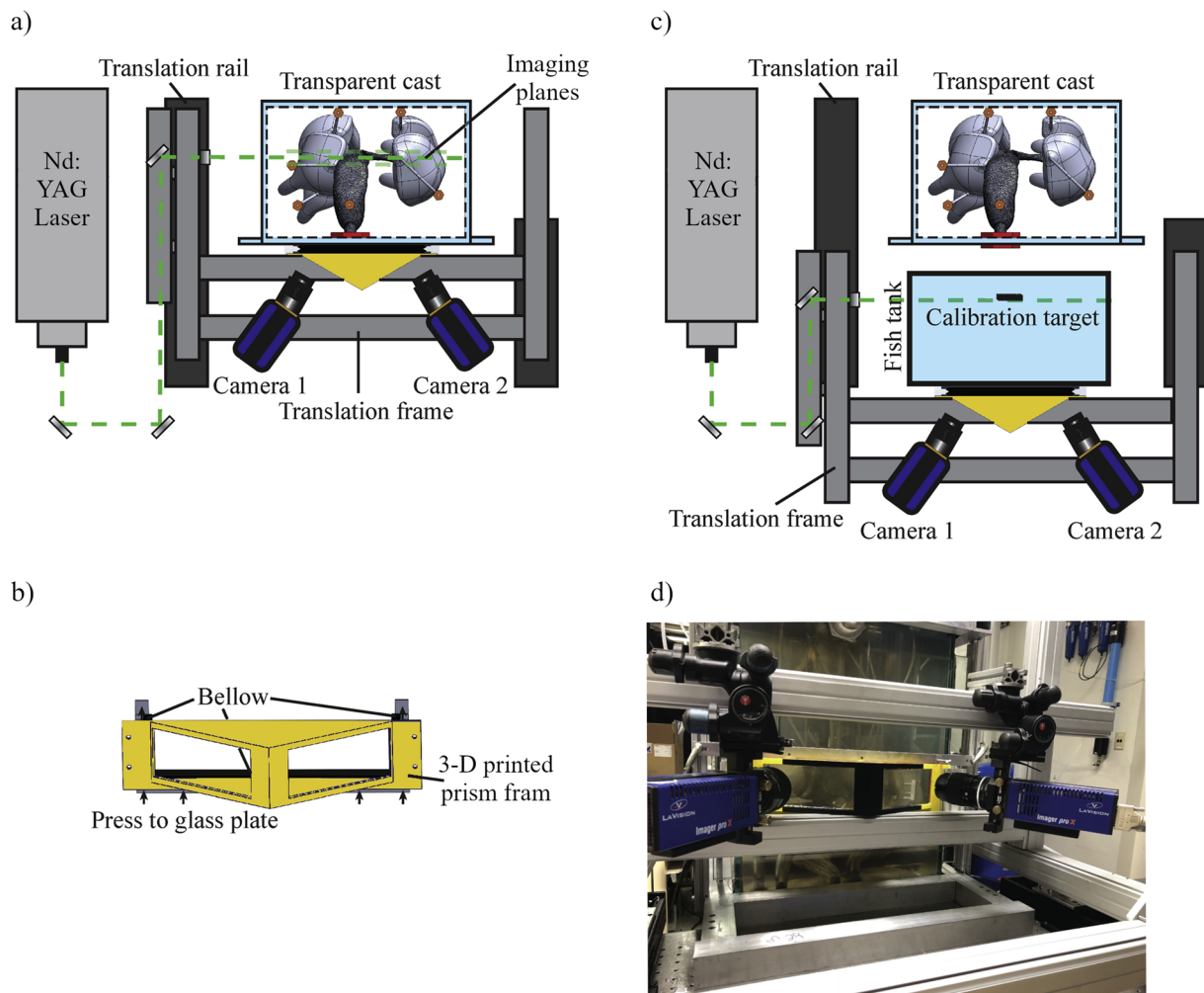

Fig. 2. Experimental setup used to acquire stereoscopic particle image velocimetry measurements. a) The optical setup and traverse system for image acquisition. b) Structure of the customized 3-D printed prism frame attached to the front face of the tank with a bellow. c) Camera calibration setup with the cameras translated away from the model and the calibration target placed in front of the cameras. d) A photograph of the imaging setup.

print the 3-D model, which included the lobe plena and central airway (Fig. 1b). We used a Fortus 400mc (Stratasys, Eden Prairie, MN) to fabricate the 3-D printed model with acrylonitrile butadiene styrene at a resolution of 0.33 mm. We further polished the 3-D printed model using an acetone vapor bath (Neff et al., 2018) and then secured it in a glass container. We casted the model in clear silicone (SYLGARD 184; Dow Corning, Midland, MI) and dissolved the 3-D printed material from the cured silicone, which resulted in a hollow, transparent model of the original geometry (Fig. 1c). To match the refraction index of the working liquid for the PIV experiments to that of the silicone (Budwig, 1994), we accordingly chose a water-glycerine mixture of 61% glycerine, with a density of 1155 kg/m^3 and a kinematic viscosity of 9.2×10^{-6} m^2/s. Finally, we attached a piston pump to the inlet of each lobe plenum, so that we could individually control the lobar flow fraction in each lobe plenum.

We performed stereoscopic PIV measurements of the three components of the velocity field within prescribed imaging planes. We selected hollow glass spherical particles (Potters Industries LLC, Malvern, PA) with a median diameter of 20 μm and density of 1.10 ± 0.05 g/cm^3 for the PIV measurements. We selected these particles for their density [which was similar to that of the working liquid (1.15 g/cm^3)] and size (large enough to reflect sufficient light to be visible and small enough to occupy 2–3 pixels in the recorded images). We studied the dynamic response of a single particle to ensure that the particles would faithfully track the fluid (Adrian and Westerweel, 2011). For a tracer particle subjected to a sinusoidal external flow with a frequency of 100 Hz, the normalized amplitude error was on the order of 10^{-6} and the phase error on the order of 10^{-3} degrees.

Fig. 2a shows the laser and camera setup used to acquire the stereoscopic images. We employed a Nd:YAG double-pulsed laser (NANO L; Litron Lasers Ltd., Warwickshire, England) and two 4-Megapixel cameras (Imager pro X 4 M; LaVision Inc., Ypsilanti, MI) with Nikon micro-Nikkor 60-mm lenses mounted *via* Scheimpflug mounts and separated by an angle of 60°. With the regular cube-shaped test section, prisms are necessary for reducing astigmatic aberrations. Fig. 2b shows the customized, 3-D printed prism frame, filled with the same cast silicone used for the model, attached to the front face of the tank with a bellow.

We poured the index-matched working liquid used in the model into the bellow, creating a homogeneous optical path from the prism face to the imaging plane. Calibrating this model is a challenge, because the complex geometry of the flow paths forbids *in situ* accessibility to any kind of calibration target. We solved this issue by securing the cameras, the prism, and the light-sheet optics onto a rigid optical frame and precisely controlled traverser (minimum measurable incremental distance of 0.1 mm). We aligned the laser beam to be parallel with the traverse translation direction, so that the relative position and orientation between the cameras and the light sheet remained the same during translation. Fig. 2c shows the setup used for calibration, which we performed by translating all of the fixed optical components away from the model and placing an aquarium filled with the same working liquid in between them. We then placed the calibration target in the tank and aligned it with the laser light sheet, providing an optical mapping for any distortion in the path. We completed the final registration using the self-calibration procedure with the collected PIV images (Wieneke, 2005), which removed any residual alignment errors between the calibration target and the light sheet.

The translation frame, combined with the customized prism, also provided the option to translate the imaging plane to different out-of-plane positions while maintaining an identical optical viewing path. Thus, we only performed camera calibration and self-calibration one time each. We repeated calibration to check for consistency and ensure that nothing was disturbed during a given test sequence. We measured flow fields at different imaging planes to provide a better understanding of the volumetric flow characteristics in a statistical sense. We acquired images and calculated instantaneous velocity vectors with DaVis 8.2

(LaVision Inc., Ypsilanti, MI). The calculation process involved an iterative multi-resolution method, starting with a first pass using a coarse interrogation window of 64 × 64 pixels, followed by a higher-resolution pass using a window of 32 × 32 pixels with an overlap of 50%. This represented a spatial resolution of approximately 0.55 mm × 0.55 mm for the interrogation cell, which varied slightly with the exact magnification at different measurement locations. We selected the time interval between image pairs to allow a maximum displacement of 12 pixels in the region of interest, which corresponds to an interface time of 300 μs. With a conservative performance estimate of 0.1 pixels for the subpixel interpolation, this gives a typical dynamic range of over 100 for the velocity measurement. We assessed interrogation quality by examining the number of spurious vectors in a single realization. Spurious vectors were identified after each intermediate and final pass using the standard normalized median test, which has been shown to be very effective at identifying random noise signals within resolved PIV data (Westerweel and Scarano, 2005). For a single realization, the ratio of the spurious vectors detected in the final pass to the total number of vectors within the masked region of measurement is typically within 2–3%, which indicates an excellent image quality.

We observed unsteady flow structures in the PIV velocity field measurements, consistent with a transition toward a turbulent state. To assess the convergence of our reported mean velocities, we acquired more than 700 independent PIV velocity field measurements each measurement location, where we selected the position with the largest degree of variability and determined the convergence speed of the mean velocity, as this position is expected to show the lowest convergence speed in the velocity field. Fig. 3 shows that after about 250 images, the velocity magnitude remains within a band of ± 5%, indicating an approximate level of convergence of mean values within this range. In addition, we determined 95% confidence intervals of the velocity magnitude at the four cross-sections (a-a', b-b', c-c', d-d') specified in Fig. 5. The 95% confidence interval at each point is obtained using: $V - \frac{k\sigma}{\sqrt{n}} \leq \mu \leq V + \frac{k\sigma}{\sqrt{n}}$, where μ represents the true local mean velocity magnitude, V is the sample population local mean value of the velocity, σ is the standard deviation of the velocity magnitude, n is the number of instantaneous velocities being averaged (n = 700) and k corresponds to the 95% confidence level with a value of 1.96 being used. We found that the maximum uncertainty band represented by this
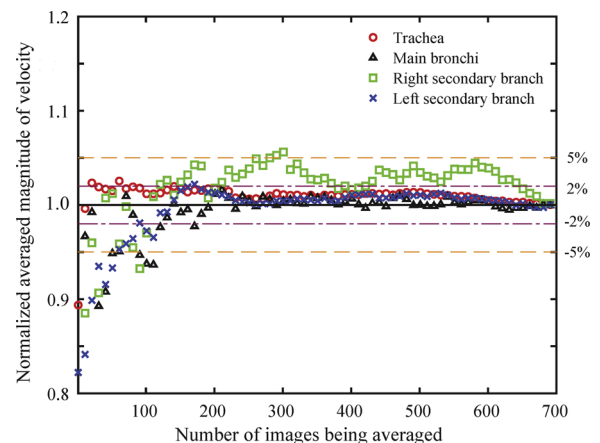

Fig. 3. The local mean velocity magnitude obtained from particle image velocimetry measurements averaged over an increasing number of instantaneous velocities and normalized by the corresponding local mean velocity averaged over all of the 700 velocity fields. The normalized averaged velocity magnitude varied over the first 250 collected field measurements, before stabilizing within a band of ± 5%, indicating a statistical convergence of the local mean velocity magnitude. This indicates that 700 velocity fields were sufficient to describe the mean velocity field.

estimate, normalized by the spatially averaged velocity of the corresponding profile, was less than ± 3.6% throughout the measurement planes.

2.3. Numerical methods

We performed CFD simulations with conditions matching those used in the PIV experiments. We calculated the Reynolds number in the trachea to be ~3500 (Re = 4Q/πDυ, for a total flow rate Q of 770.4 mL/s, tracheal diameter D of 3 cm, and kinematic viscosity υ [of the water-glycerin mixture] of 9.2×10^{-6} m^2/s). This Reynolds number is in the transitional regime, and we consequently evaluated both large eddy simulation (LES) and Reynolds-averaged Navier–Stokes (RANS) turbulence models for incompressible flows to address their suitability of reproducing experimentally observed flow patterns. For the LES model, we used a dynamic Smagorinsky–Lilly representation for the sub-grid scale (Germano et al., 1991; Lilly, 1992). For the RANS model, we employed the shear stress transport k–ω turbulence method (Menter, 1994).

We used the fluid properties of the water-glycerin mixture from the PIV experiments. We applied no-slip boundary conditions on the walls of the domain and a boundary condition of zero gauge pressure at the outlet. We specified uniform velocity profile boundary conditions at each lobe plenum inlet where the velocity magnitude was determined from the corresponding flow condition and lobar flow fraction. Flow is distributed within the plena and to the distal branches of the patient-specific geometry without specifying flow rates at each branch inlet. When using the RANS model, we also specified a turbulence intensity of 5% and a turbulence length scale of 0.2 cm at each lobe plenum inlet.

We numerically solved the equations of fluid flow using the finite-volume based solver FLUENT (version 18.0.0; ANSYS Inc., Canonsburg, PA), with a second order central-differencing scheme for the convective terms. For the RANS model, we performed steady-state calculations with a coupled method for the pressure-velocity coupling. For the LES model, we used a fractional step method for the pressure-velocity coupling and performed transient calculations with a time step Δt of 10^{-4} s, ensuring the Courant–Friedrichs–Lewy number was less than one throughout the computational domain. We began collecting flow statistics after the flow developed in the trachea, and averaged the subsequent flow over a 2 s period to yield statistically steady velocity and pressure fields.

Using ICEM CFD (version 18.0; ANSYS Inc. Canonsburg, PA), we generated unstructured, tetrahedral meshes where the near-wall region featured high-resolution mesh layers that transitioned to coarser cells in the interior of the computational domain. We first created an Octree-type mesh for the surface and extruded 10 prism layers in the near-wall region featuring a thickness of 0.1 mm. Then, we filled the remaining mesh volume utilizing the advancing front method. To ensure a high-quality mesh, we smoothed the mesh so that the skewness for each cell was less than 0.8 and the orthogonality quality was greater than 0.5.

We performed a grid independence test by examining the velocity magnitude and turbulent kinetic energy values located along the centerline of the midplane of the trachea. We examined two different mesh configurations, each with 10 mesh layers in the near-wall region featuring a thickness of 0.1 mm, but different spatial resolutions in the interior of the domain (1.0 or 0.75 mm in the bulk of the flow consisting of 18.3 million or 24.7 million cells, respectively). The velocity magnitude values showed a relative difference of less than 2% across the centerline of the midplane of the trachea, where the maximum differences were 1.58 and 1.55 m/s for the 1.0- and 0.75-mm meshes, respectively. In addition, the turbulent kinetic energy in the trachea varied by a relative difference of less than 1%, where the maximum differences were 0.283 and 0.281 m^2/s for the 1.0- and 0.75-mm meshes, respectively. Hence, we chose the mesh configuration with a resolution of 1.0 mm. We ran simulations on 256 CPU cores of the Excalibur cluster at the U.S. Department of Defense Supercomputing Resource Center, located at the U.S. Army Research Laboratory in Adelphi, MD.

2.4. Measure of flow pattern similarity

We quantified the similarity of flow patterns with Pearson correlation coefficients and root-mean-square differences for the velocity field in chosen planes of the computational domain. The Pearson correlation coefficient (R) between two velocity fields $\boldsymbol{u}(\boldsymbol{x})$ and $\boldsymbol{v}(\boldsymbol{x})$ in the measurement plane Ω is defined as:

$$R = \frac{\int_\Omega (\boldsymbol{u}(\boldsymbol{x}) - \bar{\boldsymbol{u}}) \cdot (\boldsymbol{v}(\boldsymbol{x}) - \bar{\boldsymbol{v}}) dx}{(\int_\Omega (\boldsymbol{u}(\boldsymbol{x}) - \bar{\boldsymbol{u}}) \cdot (\boldsymbol{u}(\boldsymbol{x}) - \bar{\boldsymbol{u}}) dx \int_\Omega (\boldsymbol{v}(\boldsymbol{x}) - \bar{\boldsymbol{v}}) \cdot (\boldsymbol{v}(\boldsymbol{x}) - \bar{\boldsymbol{v}}) dx)^{1/2}}$$

(1)

where $\bar{\boldsymbol{u}}$ and $\bar{\boldsymbol{v}}$ denote the velocity fields averaged over the plane Ω and · represents the dot product. R indicates the pattern similarity in the measurement plane, but does not take into account velocity magnitude differences. The root-mean-square difference (D_{rms}) between two velocity fields $\boldsymbol{u}(\boldsymbol{x})$ and $\boldsymbol{v}(\boldsymbol{x})$ in the measurement plane Ω is defined as:

$$D_{rms} = \left(\frac{\int_\Omega (\boldsymbol{u}(\boldsymbol{x}) - \boldsymbol{v}(\boldsymbol{x})) \cdot (\boldsymbol{u}(\boldsymbol{x}) - \boldsymbol{v}(\boldsymbol{x})) dx}{A} \right)^{1/2}$$

(2)

where A denotes the area of the plane Ω. D_{rms} takes into account both magnitude differences and pattern similarity in the measurement plane. For both metrics, we compared the intermediate and severe conditions to the normal condition to identify any differences in the flow field associated with the disease condition.

3. Results

3.1. Flow unsteadiness

We obtained PIV measurements of flow in the full model geometry (Fig. 1b) under steady exhalation conditions at a flow rate Q of 770.4 mL/s for the normal condition in Table 1 (note that for air in a human scale geometry, this corresponds to Q = 600 mL/s and Re ≈ 3500 in the trachea). The PIV measurements exhibited fluctuations over time at all locations; these fluctuations did not decay despite the constant flow rate, suggesting that the flow was inherently unsteady. We characterized the unsteadiness with the turbulence intensity, I = u′/U$_T$, where u′ is the root-mean-square of the velocity fluctuations and U$_T$ = 1.5 m/s is the bulk velocity in the trachea. Fig. 4 shows plots of turbulence intensity values for the PIV measurements averaged over the 700 velocity fields. The turbulence intensity showed considerable fluctuations at all four measurement locations, with I values greater than 10% occurring at all locations. The trachea (Fig. 4, location A) showed a relatively uniform distribution of I, with a small reduction as the flow exited the measurement plane. The main bronchi (Fig. 4, location B) showed an increase in I associated with the formation of a jet in the left branch. The right secondary branch (Fig. 4, location C) exhibited quite complex behavior where the branches merge, leading to the highest observed degree of fluctuations. Similarly, the left secondary branch (Fig. 4, location D) showed an increase in I in the vicinity of where the branches merge, although the behavior was less complex than that in the right secondary bifurcation.

3.2. Validation

We predicted flow fields using the LES and RANS models with the same flow conditions as the PIV measurements and then compared the predictions with the measurements to validate our CFD model. Fig. 5a shows a comparison of the mean flow for the PIV measurements, the LES model (averaged over a 2 s period), and the RANS model (at steady state). Overall, the LES model showed better agreement with the PIV measurements than did the RANS model. The PIV measurements in the
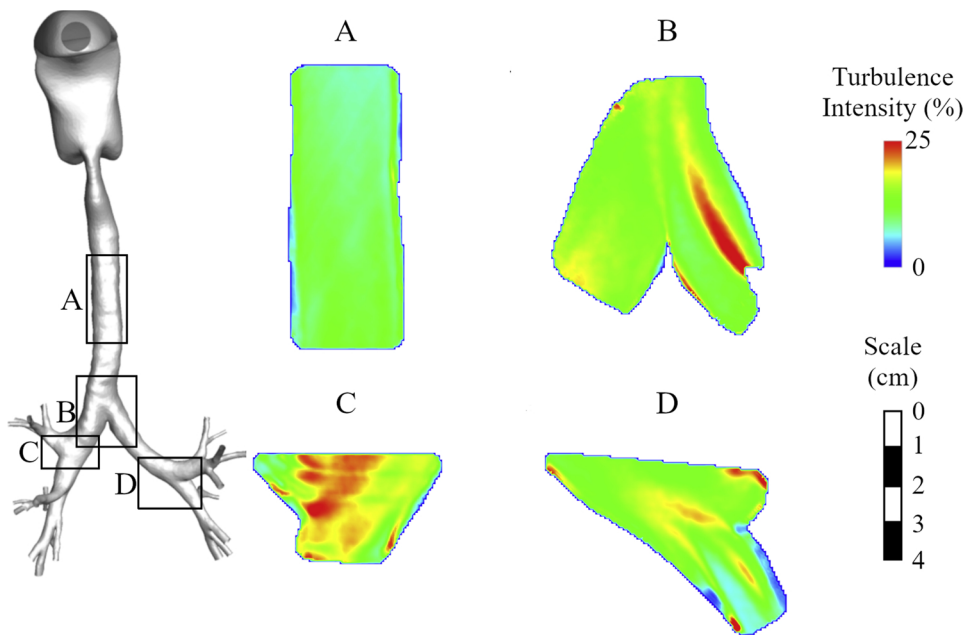
Fig. 4. Contours of mean turbulence intensity values from the particle image velocimetry experiments averaged over 700 velocity fields at four measurement locations (A, trachea; B, main bronchi; C, right secondary bronchi; and D, left secondary bronchi). Turbulence intensity I is defined as u'/U_T, where u' denotes the root-mean-square of the velocity fluctuations and U_T ($=1.5\,m/s$) represents the bulk velocity in the trachea. At all locations, the values of I are greater than 10%, indicating that the flow field is inherently unsteady. The plots of I reveal marked fluctuations in the right and left secondary branches (locations C and D) suggesting that the sources of unsteadiness are in the smaller branches of the central airway. Local geometric features of the branches, *e.g.*, branch curvature or a change in cross-sectional shape, are likely to initiate the formation of turbulent structures that intensify when flows merge at branch bifurcations.

trachea (Fig. 5a, location A) exhibited a blunted flow profile, which the LES model captured, but for which the RANS model predicted a skewed profile with a peak velocity magnitude displaced from the centerline of the trachea. Similarly, compared with the RANS model, the LES model showed better agreement with the PIV measurements in the main bronchi (Fig. 5a, location B). The PIV measurements showed the formation of a jet and separation region in the left branch of the main bronchi, which both models predicted. PIV measurements in the right branch of the main bronchi exhibited an asymmetric profile with an increase in velocity magnitude towards the left boundary of the right branch. The LES model predicted two peaks that dissipated near the bifurcation of the main bronchi, whereas the RANS model predicted two peaks that continued beyond the bifurcation.

The LES and RANS models produced comparable predictions in the right secondary branch (Fig. 5a, location C). PIV measurements in the right secondary branch showed a recirculation region near the bifurcation of the right branch. Whereas both models predicted this recirculation region to be quite wide, the corresponding region was quite narrow for the PIV measurements. Both models also predicted two peaks that reached the main bronchi, which were not seen in the PIV measurements. Furthermore, in the left secondary branch (Fig. 5a, location D), both models predicted a peak in velocity magnitude that formed towards the center of the lower branch and connected to a region of increased velocity magnitude past the bifurcation of the left branch, consistent with the PIV measurements.

Fig. 5b shows plots of the mean velocity magnitude profiles along specified lines indicated in Fig. 5a, which offer more detailed comparisons of the velocity magnitude. Overall, the LES model showed good agreement with the PIV measurements, except for the right secondary branch (Fig. 5b, c-c′). The RANS model predictions showed good agreement with the PIV measurements in the left secondary branch (Fig. 5b, d-d′), but showed notable differences at all other locations. Consequently, we chose the LES model to generate predictions for the following results.

3.3. Lobar flow fractions

We predicted flow profiles with the LES model under steady exhalation conditions averaged over a 2 s period for the three flow conditions listed in Table 1: normal, intermediate, and severe. We used the full model geometry with plena attached to the central airway (Fig. 1b)

and a constant flow rate Q of 770.4 mL/s for all three conditions. Because Q was fixed, the Reynolds number in the trachea (Re $= 4Q/\pi D\upsilon \approx 3500$) was the same for all flow conditions. However, the Reynolds number in the branches of the lower airways varied between flow conditions due to the alteration in flow fractions.

Fig. 6 shows contours of the mean velocity magnitude in planes taken throughout the left main bronchus and secondary branches. Table 2 shows the computed values of R and D_{rms} comparing both the intermediate and severe flow conditions to the normal condition for the corresponding planes in Fig. 6. For the intermediate condition, the flow was highly correlated ($R \geq 0.98$) with that of the normal condition in the lower branches (Fig. 6, locations D and E) and became less correlated ($0.84 \leq R \leq 0.87$) as it developed along the main bronchus, where the correlation became minimal ($R = 0.80$) at the uppermost slice of the main bronchus (Fig. 6, location A). The values for D_{rms} also showed the largest difference ($D_{rms} = 0.54\,m/s$) at the uppermost slice due to the skewness of the flow as it developed along the curved main bronchus. For the severe condition, we observed a similar trend for R, although the correlation was smallest ($R = 0.67$) at the location near the bifurcation of the left main bronchus (Fig. 6, location C). Because the flow is highly correlated in the secondary branches ($R \geq 0.98$), this decreased correlation is due to the increased difference between flow fractions from the left upper and left lower lobes, where the merging flows produce a different flow pattern. At higher slices along the left main bronchus (Fig. 6, locations A and B) the flow showed a slight increase in correlation with that in the normal condition ($R = 0.72$), although the correlation was less than that of the intermediate condition with the normal condition ($0.80 \leq R \leq 0.87$). The value of D_{rms} became maximal at the uppermost slice of the main bronchus (Fig. 6, location A), and all values of D_{rms} showed greater differences with the normal condition than did those of the intermediate condition.

Fig. 7 shows contours of the mean velocity magnitude in planes taken throughout the right main bronchus and secondary branches with corresponding values of R and D_{rms} in Table 3 comparing the intermediate and severe flow conditions to the normal flow condition. The intermediate condition was highly correlated ($R \geq 0.95$) with the normal condition at locations in the secondary branches (Fig. 7, locations C, D, and E), but the flow patterns became considerably less correlated ($R \leq 0.60$) in the right main bronchus (Fig. 7, locations A and B). Compared to the left main bronchus, the right main bronchus showed significantly less correlation due to the
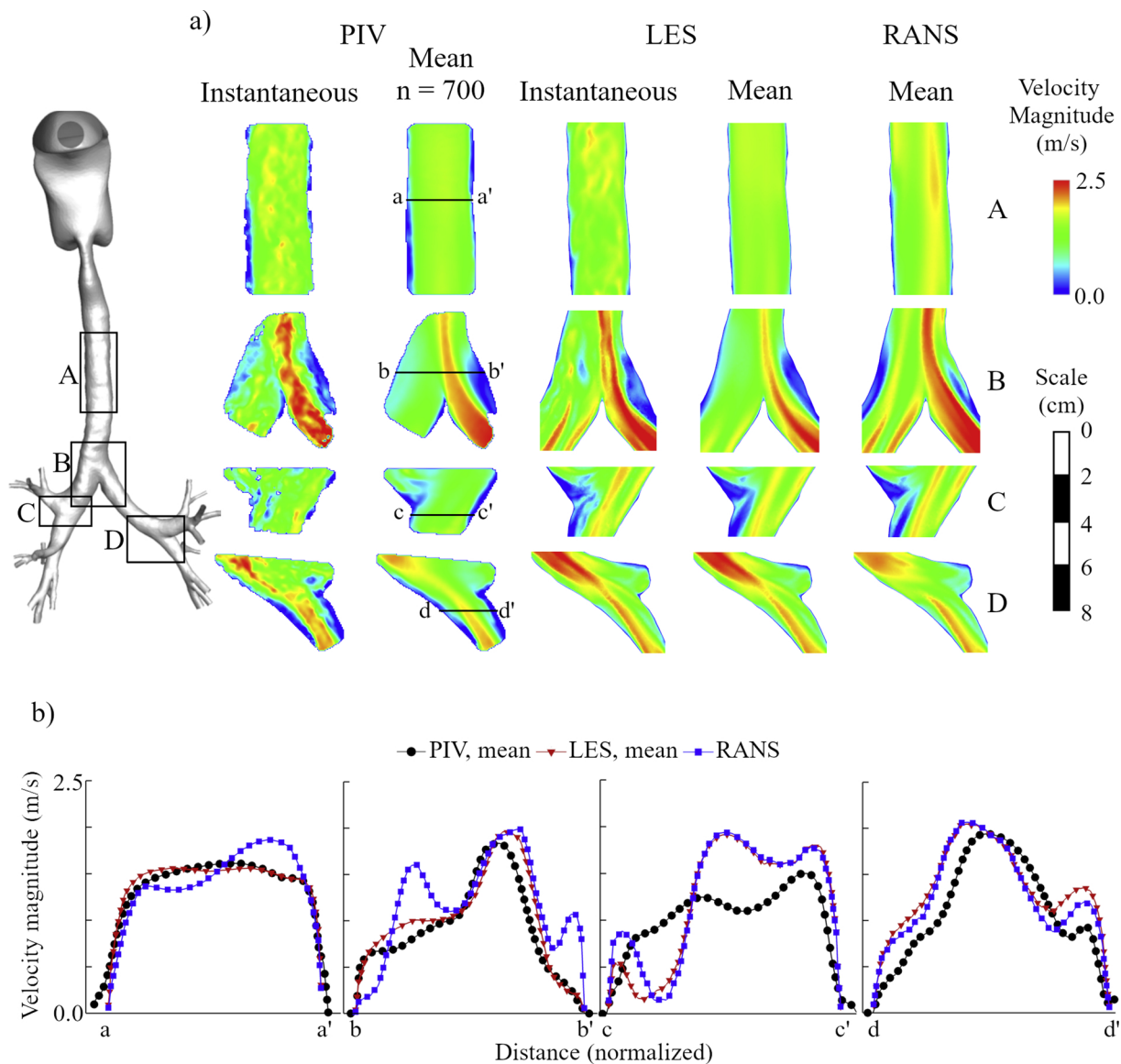
Fig. 5. Comparison of particle image velocimetry (PIV) experiments, large eddy simulation (LES) predictions, and Reynolds-averaged Navier–Stokes (RANS) predictions. a) Contours of the velocity magnitude at four measurement locations (A, B, C, and D) for the instantaneous and mean flows. Instantaneous flows obtained at an arbitrary time point demonstrated marked variations in the flow field over time. These fluctuations were the result of mixing behavior that occured when streams merged near bifurcations. The experimentally observed flow patterns, particularly those at locations A and B, were captured more accurately by the LES model than by the RANS model. At locations C and D, the models performed similarly, where both failed to reproduce the complex recirculation region at location C but captured the observed pattern at location D. b) Cross-sectional velocity magnitude profiles for the averaged flow at the four measurement locations, providing a detailed view of the comparison between the PIV, LES, and RANS. In the trachea (a-a') and first bifurcation (b-b'), the predictions of the LES model resembled the PIV measurements more closely than do those of the RANS model, which predicts off-centerline peaks not observed in the PIV measurements. In the right and left secondary bifurcations, the predictions for the LES and RANS models were nearly identical. The dimensional length is 2.9 cm between points a and a', 4.2 cm between b and b', 2.8 cm between c and c', and 2.5 cm between d and d'.

increased cross-sectional area of the bronchus. Despite the highly correlated flow pattern in the right upper branch (Fig. 7, location C), this location exhibited the maximum value for $D_{rms} = 0.71$ m/s because of the significant increase in velocity magnitude. For the severe condition, only one location showed a high correlation ($R = 0.93$) with the normal condition (Fig. 7, location C), with all other locations showing lower correlations ($0.39 \leq R \leq 0.76$). In the right lower branches (Fig. 7, locations D and E), the decrease in flow fraction produced larger regions of decreased velocity magnitude, which led to the reduced correlation with the normal condition. However, D_{rms} still became maximal ($D_{rms} = 1.40$ m/s) in the right upper branch (Fig. 7, location C) because of the marked increase in flow fraction.

Fig. 8 shows contours of the mean velocity magnitude in transverse

slices of the trachea, and Table 4 contains the associated values of R and D_{rms} comparing the intermediate and severe flow conditions to the normal flow condition. In the intermediate condition, the flow became more correlated with that in the normal condition as it developed along the length of the trachea, attaining a minimum correlation ($R = 0.80$) at the middle plane (Fig. 8, location B). We observed a similar trend for the severe condition, although the correlation became minimal ($R = 0.81$) at the lowest plane (Fig. 8, location C). In both conditions, however, the flow became similarly correlated ($R \geq 0.94$) with the normal condition at the uppermost plane (Fig. 8, location A) as the flow developed along the length of the trachea. Similarly, in both conditions, D_{rms} became maximal ($D_{rms} = 0.31$ m/s for the intermediate condition and $D_{rms} = 0.37$ m/s for the severe condition) at the lowest slice (Fig. 8,
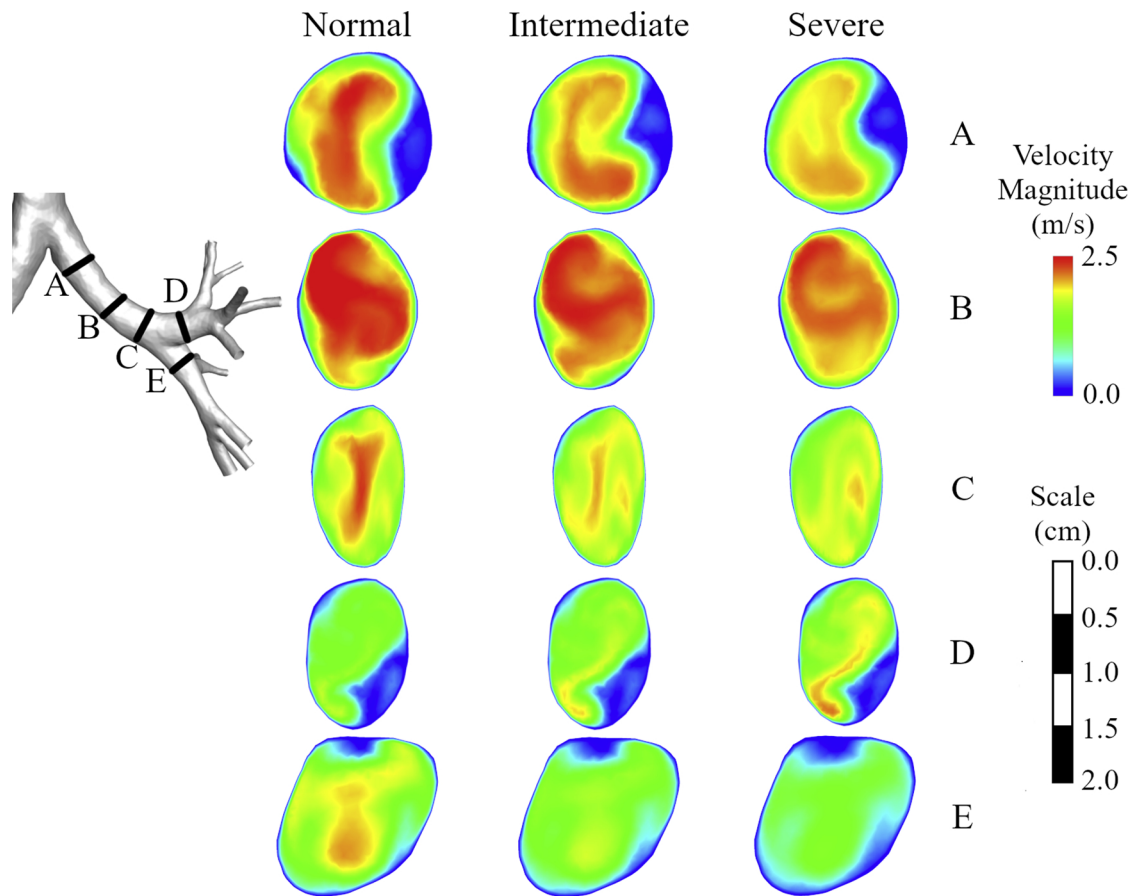
Fig. 6. Comparison of mean velocity magnitude contours in measurement planes taken throughout the left main bronchus and secondary branches for the normal, intermediate, and severe flow conditions. At locations D and E, flow patterns across the flow conditions were highly correlated but of different magnitude. As the flow merged at the branch bifurcation then developed along the curvature of the main bronchus, the alteration to lobar flow fractions resulted in differing flow patterns.

Table 2
Computed Pearson correlation coefficient (R) and root-mean-square differences (D_{rms}) between intermediate and normal flow conditions (Intermediate) and between severe and normal conditions (Severe) for the measurement locations indicated in Fig. 6.

Measurement Location	R		D_{rms} (m/s)	
	Intermediate	Severe	Intermediate	Severe
A	0.80	0.72	0.54	0.63
B	0.84	0.72	0.39	0.53
C	0.87	0.67	0.31	0.50
D	0.99	0.98	0.18	0.36
E	0.99	0.98	0.29	0.58

location C) because of the large variation in velocity magnitude across the plane.

Fig. 9 shows the spatial distribution of correlation coefficients taken from Tables 2–4 throughout the central airway. For the intermediate condition, the flow patterns were highly correlated ($R \geq 0.94$) with the normal condition at the upper-most plane in the trachea and planes in the secondary branches of both the left and right main bronchi. The correlation decreased throughout the main bronchi ($0.56 \leq R \leq 0.87$), becoming lowest in the right main bronchus ($R = 0.56$). The severe condition showed a similar distribution of correlation coefficients throughout the majority of the central airway, except for planes in the lower right branches. The flow in these planes were highly correlated ($R \geq 0.95$) between the intermediate and normal conditions but considerably less correlated ($0.65 \leq R \leq 0.76$) between the severe and normal conditions. In addition, the correlation decreased at most

measurement planes for the severe condition ($0.39 \leq R \leq 0.98$) compared to the intermediate condition ($0.56 \leq R \leq 0.99$), except at two planes in the trachea ($0.80 \leq R \leq 0.94$ for the intermediate condition and $0.88 \leq R \leq 0.95$ for the severe condition).

4. Discussion

We validated a CFD model of flow with PIV measurements for a single flow condition under steady exhalation. We then utilized the CFD model to predict flow patterns for two more flow conditions by altering the lobar flow fractions to represent the effect of obstructions in the lower airways on flow distribution. Subsequently, we measured the correlation of the flow patterns by computing Pearson correlation coefficients and root-mean-square differences at multiple measurement planes throughout the central airway.

4.1. Flow unsteadiness in PIV measurements

We performed PIV measurements with a constant flow rate and observed flow unsteadiness, consistent with earlier studies (Dekker, 1961). We characterized this unsteadiness by the turbulence intensity, which was pronounced at all measurement locations within the central airway ($I > 10\%$). Previous studies of inhalation showing that flow unsteadiness occurs in patient-specific geometries (Zhang and Kleinstreuer, 2004; Xi et al., 2008; Choi et al., 2009; Bernate et al., 2017) have attributed it to the laryngeal jet, which generates turbulent structures that convect deeper into the lung. For exhalation, however, a different mechanism must be responsible for generating the unsteadiness. The marked fluctuations observed in the right and left secondary
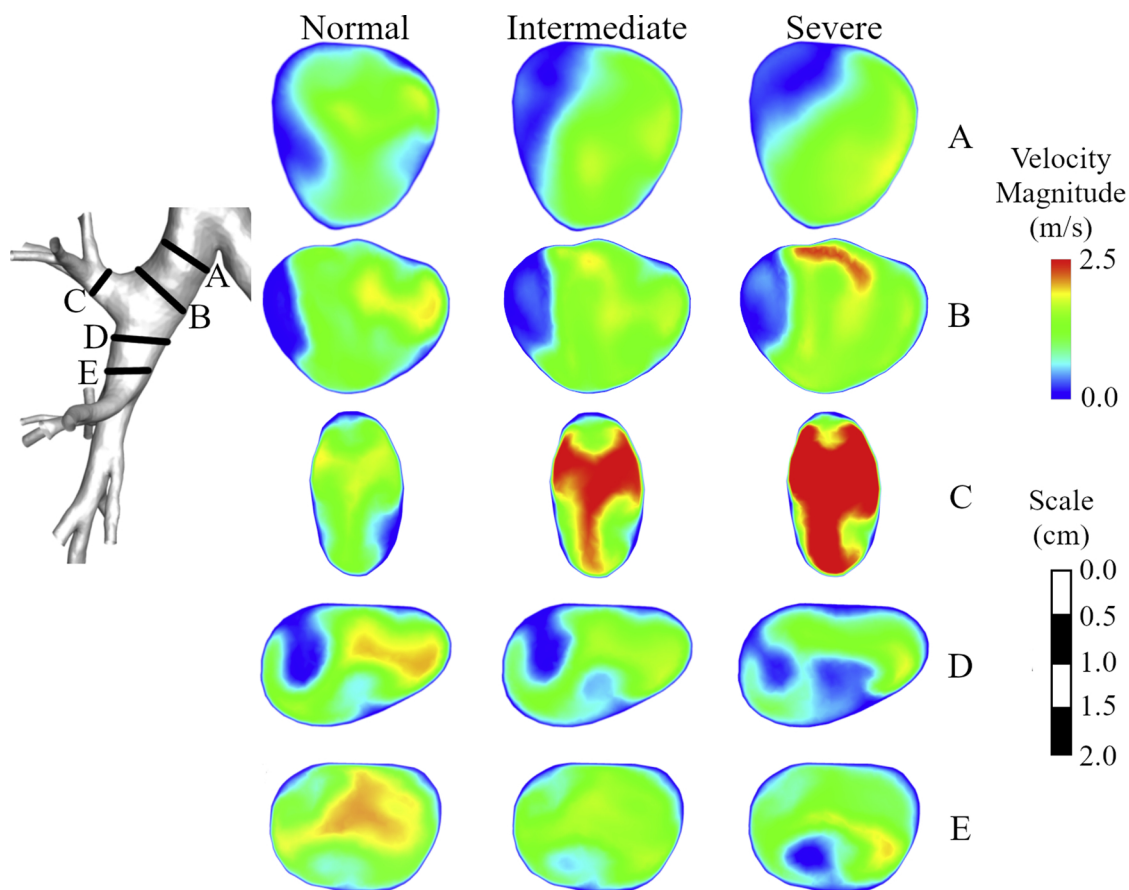
Fig. 7. Comparison of mean velocity magnitude contours in measurement planes taken throughout the right main bronchus and secondary branches for the normal, intermediate, and severe flow conditions. At location C, flow patterns were highly correlated with differing magnitudes across all flow conditions, but at locations D and E, the flow patterns in the severe condition became less correlated with the normal and intermediate conditions. The cross-sectional area of the measurement plane significantly increased at locations A and B, resulting in flow patterns with a low correlation.

Table 3

Computed Pearson correlation coefficient (R) and root-mean-square differences (D_{rms}) between intermediate and normal flow conditions (Intermediate) and between severe and normal conditions (Severe) for the measurement locations indicated in Fig. 7.

Measurement Location	R		D_{rms} (m/s)	
	Intermediate	Severe	Intermediate	Severe
A	0.56	0.39	0.52	0.65
B	0.60	0.54	0.53	0.78
C	0.96	0.93	0.71	1.40
D	0.96	0.65	0.26	0.60
E	0.95	0.76	0.30	0.60

branches (Fig. 4, locations C and D) suggest that the source of unsteadiness is in the smaller branches of the central airway. A likely possibility is that the local geometric features of the branches, *e.g.*, branch curvature or change in cross-sectional shape, initiate the formation of turbulent structures that intensify when flows merge at branch bifurcations.

4.2. Suitability of turbulence models

We evaluated both LES and RANS models in the central airway geometry and compared their predictions to PIV measurements. The LES model was more accurate in the larger airways (Fig. 5a, locations A and B), although both models performed similarly in the right and left secondary branches (Fig. 5a, locations C and D). In particular, the LES

model captures the mixing behavior observed in the trachea that results from the merging of streams in the main bronchi. However, the LES model is more computationally intensive than the RANS model, and there may be occasions when use of the RANS model is sufficient.

4.3. Flow patterns

We predicted flow patterns in the central airway for three flow conditions (Figs. 6–8), and then measured the correlation between the predicted flow patterns for the intermediate and normal conditions as well as those for the severe and normal conditions (Tables 2–4, Fig. 9). For locations in the secondary branches of the bronchi (Fig. 6, locations D and E; Fig. 7, location C), we observed a high correlation ($R \geq 0.93$) between the normal and intermediate conditions and between the normal and severe conditions. This indicates that the influence of flow rate is negligible at these locations, likely because of the dominance of streamwise velocity components. However, in the lower right branch (Fig. 7, locations D and E), we observed a transition where the correlation between the intermediate and normal conditions was high ($R \geq 0.95$), whereas correlation between the severe and normal conditions was not ($0.65 \leq R \leq 0.76$). This suggests the presence of a transition point at which secondary flows become more apparent as the flow rate decreases, and the flow patterns show a greater difference. Because of this transition, lower total flow rates would be optimal in differentiating flow conditions.

We observed the greatest flow pattern differences ($0.39 \leq R \leq 0.87$) in the main bronchi (Fig. 6, locations A, B, and C; Fig. 7, locations A and B). Although the flow patterns generated in the
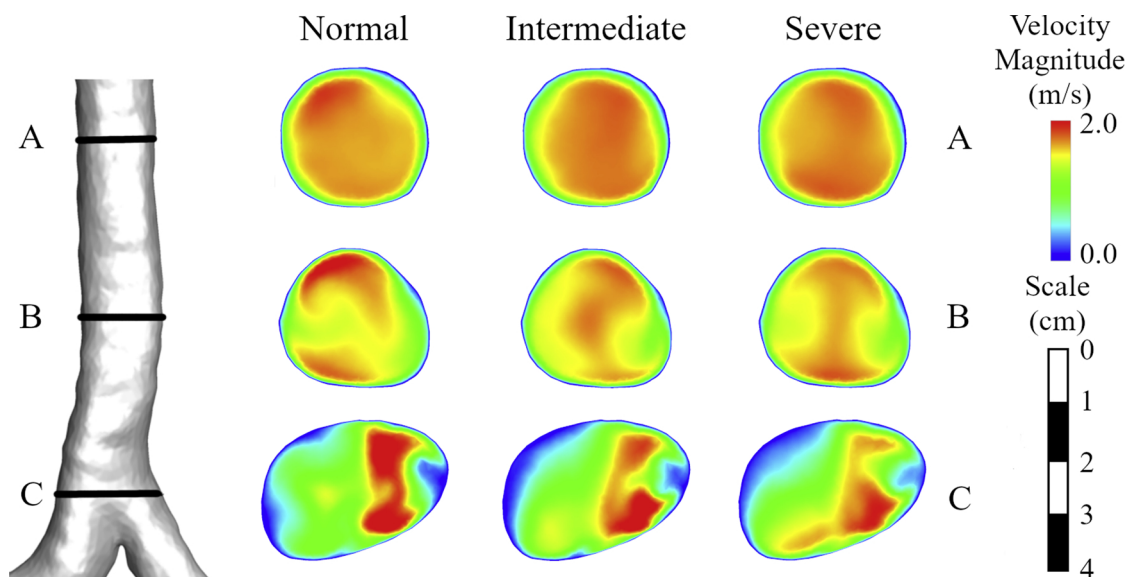
Fig. 8. Comparison of mean velocity magnitude contours in transverse slices through the trachea for the normal, intermediate, and severe flow conditions. The flow patterns showed the least correlation at location C; they then developed along the length of the trachea and became highly correlated at the uppermost plane at location A.

Table 4

Computed Pearson correlation coefficient (R) and root-mean-square differences (D_{rms}) between intermediate and normal flow conditions (Intermediate) and between severe and normal conditions (Severe) for the measurement locations indicated in Fig. 8.

Measurement Location	R		D_{rms} (m/s)	
	Intermediate	Severe	Intermediate	Severe
A	0.94	0.95	0.15	0.13
B	0.80	0.88	0.26	0.20
C	0.86	0.81	0.31	0.37

secondary branches are highly correlated ($R \geq 0.93$), the flow fractions are different. Hence, when the flow patterns merge past the bifurcation with differing strengths, a different pattern is generated. This is most evident when comparing the intermediate condition to the normal condition ($0.56 \leq R \leq 0.60$) in the right main bronchi (Fig. 7, locations A and B). However, the correlation dissipated as the flow reached the trachea, where the streamwise flow dominated and the flow developed along the length of the trachea to be nearly indistinguishable ($R \geq 0.94$) between the conditions (Fig. 8, location A).

These predictions suggest that although flow patterns in the central airway can identify flow abnormalities in the lung, the choice of measurement location is critical to differentiating flow conditions. This stands in contrast to the results obtained for idealized airways by Sul et al. (2018), which indicate a more robust spatial distribution of flow pattern variation throughout the airway. Specifically, their results exhibit significant differences in flow patterns in the secondary branches of the lung between healthy and diseased flow conditions, which were less evident in the current study. However, their results also indicate that the maximum flow pattern differentiation is attained at the main bronchi, consistent with our predictions. Taken together, both sets of predictions suggest that the main bronchi should be the focus of further investigations, as this is where we observed the greatest differences in flow patterns. Another factor that complicates the use of flow patterns to differentiate flow conditions is the presence of flow unsteadiness in the patient-specific geometry. Given the observed unsteadiness, measurement of flow patterns would require multiple breathing cycles to capture the mean flow.

However, the flow pattern predictions presented here are limited in

scope. In the present study, we used a single central airway geometry and evaluated the effect of lobar flow fractions on flow patterns. Lung structure among patients is highly variable, and this variability will further influence the observed flow patterns, even among healthy patients. Furthermore, we assumed the airways were rigid, but the airways deform during the breathing cycle, which would also likely influence flow patterns. Lastly, we used a steady exhalation condition for this study, and alterations to flow rate throughout the breathing cycle will certainly influence flow patterns when combined with the observed unsteadiness. Despite these limitations, our study found that flow patterns corresponding to altered lobar flow fractions in a single lung geometry differentiate primarily in the main bronchi, and we expect these findings to be reproducible for any given, single lung geometry. That is, for a single lung geometry, alterations to lobar flow fractions will significantly influence flow patterns in the main bronchi.

5. Summary

In this study, we numerically examined flow patterns of a patient-specific geometry under steady exhalation, with boundary conditions representing the effect of obstructions in the lower airways. PIV measurements indicated that the flow was markedly unsteady. We evaluated two turbulence models, RANS and LES, for their suitability of reproducing the measured velocity fields, and found that the LES model predictions were more consistent with the PIV measurements. Subsequently, we used the LES model to predict flow patterns for three flow conditions representing subjects ranging from healthy to diseased, by altering the boundary conditions associated with the distribution of flow across the lung lobes (lobar flow fractions). We used Pearson correlation coefficients and root-mean-square differences to evaluate flow pattern similarity between the flow conditions. Flow patterns showed differentiation across the flow conditions, primarily with low correlations in the right main bronchi ($R \leq 0.60$) high correlations in the secondary branches and the uppermost region of the trachea ($R \geq 0.90$). These results indicate that flow patterns are useful for differentiating flow conditions, but that this depends critically on the choice of measurement location.
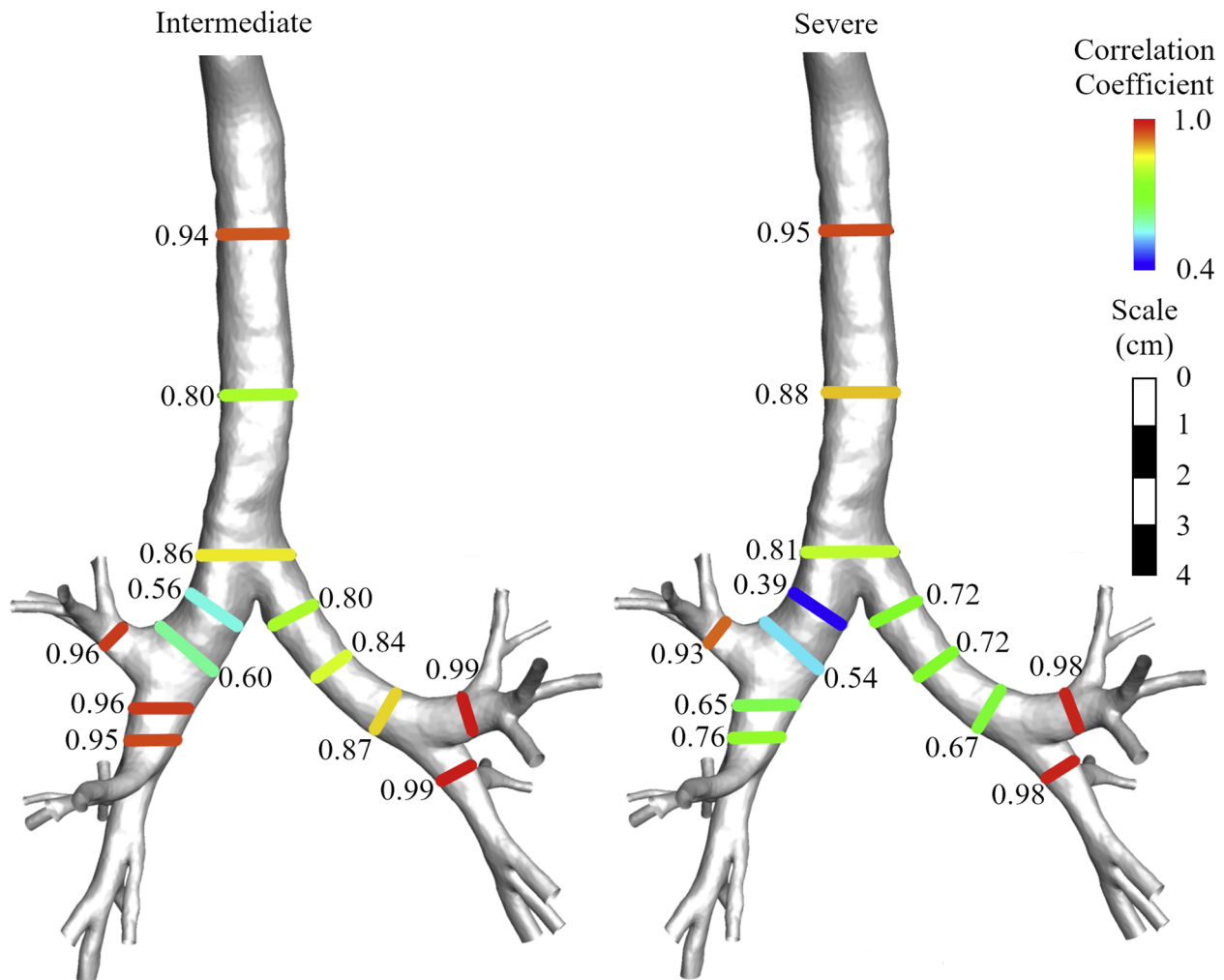
Fig. 9. Spatial distribution of Pearson correlation coefficients between (left) healthy and intermediate flow conditions and between (right) healthy and severe flow conditions. Flow patterns were least correlated in the right main bronchi and highly correlated in the secondary branches and regions of the trachea.

Disclosures

The opinions and assertions contained herein are the private views of the authors and are not to be construed as official or as reflecting the views of the U.S. Army, U.S. Department of Defense, or The Henry M. Jackson Foundation for Advancement of Military Medicine, Inc. This paper has been approved for public release with unlimited distribution.

Acknowledgments

References

Adrian, R.J., Westerweel, J., 2011. Particle Image Velocimetry. Cambridge University Press, Cambridge, UK.

Anderson, N.J., Cassidy, P.E., Janssen, L.L., Dengel, D.R., 2006. Peak inspiratory flows of adults exercising at light, moderate and heavy work loads. J. Int. Soc. Respir. Prot. 23, 53–63.

Ash, S.Y., Diaz, A.A., 2017. The role of imaging in the assessment of severe asthma. Curr. Opin. Pulm. Med. 23, 97–102.

Berg, K., Wright, J.L., 2016. The pathology of chronic obstructive pulmonary disease: progress in the 20th and 21st centuries. Arch. Pathol. Lab. Med. 140, 1423–1428.

Bernate, J.A., Geisler, T.S., Padhy, S., Shaqfeh, E.S., Iaccarino, G., 2017. Study of the flow unsteadiness in the human airway using large eddy simulation. Phys. Rev. Fluids 2, 083101.

Budwig, R., 1994. Refractive index matching methods for liquid flow investigations. Exp. Fluids 17, 350–355.

Burgel, P., 2011. The role of small airways in obstructive airway diseases. Eur. Respir. Rev. 20, 23–33.

Choi, J., Tawhai, M.H., Hoffman, E.A., Lin, C.-L., 2009. On intra-and intersubject variabilities of airflow in the human lungs. Phys. Fluids 21, 101901.

De Backer, J.W., Vos, W.G., Vinchurkar, S.C., Claes, R., Drollmann, A., Wulfrank, D., Parizel, P.M., Germonpré, P., De Backer, W., 2010. Validation of computational fluid dynamics in CT-based airway models with SPECT/CT. Radiology 257, 854–862.

Dekker, E., 1961. Transition between laminar and turbulent flow in human trachea. J. Appl. Physiol. 16, 1060–1064.

Diaz, A.A., Valim, C., Yamashiro, T., Estépar, R.S.J., Ross, J.C., Matsuoka, S., Bartholmai, B., Hatabu, H., Silverman, E.K., Washko, G.R., 2010. Airway count and emphysema assessed by chest CT imaging predicts clinical outcome in smokers. Chest 138, 880–887.

Downie, S.R., Salome, C.M., Verbanck, S., Thompson, B.R., Berend, N., King, G.G., 2007. Ventilation heterogeneity is a major determinant of airway hyperresponsiveness in asthma, independent of airway inflammation. Thorax 62, 684–689.

Germano, M., Piomelli, U., Moin, P., Cabot, W.H., 1991. A dynamic subgrid-scale eddy viscosity model. Phys. Fluids A 3, 1760–1765.

Gotway, M.B., Freemer, M.M., King, T.E., 2007. Challenges in pulmonary fibrosis · 1: use of high resolution CT scanning of the lung for the evaluation of patients with idiopathic interstitial pneumonias. Thorax 62, 546–553.

Haruna, A., Muro, S., Nakano, Y., Ohara, T., Hoshino, Y., Ogawa, E., Hirai, T., Niimi, A., Nishimura, K., Chin, K., 2010. CT scan findings of emphysema predict mortality in COPD. Chest 138, 635–640.

Hogg, J.C., Macklem, P.T., Thurlbeck, W., 1968. Site and nature of airway obstruction in chronic obstructive lung disease. N. Engl. J. Med. 278, 1355–1360.

Kitaguchi, Y., Fujimoto, K., Hanaoka, M., Kawakami, S., Honda, T., Keishi, K., 2010. Clinical characteristics of combined pulmonary fibrosis and emphysema. Respirology 15, 265–271.

Kuyper, L.M., Paré, P.D., Hogg, J.C., Lambert, R.K., Ionescu, D., Woods, R., Bai, T.R., 2003. Characterization of airway plugging in fatal asthma. Am. J. Med. 115, 6–11.

Lilly, D.K., 1992. A proposed modification of the Germano subgrid-scale closure method. Phys. Fluids A 4, 633–635.

Lin, C.-L., Tawhai, M.H., McLennan, G., Hoffman, E.A., 2007. Characteristics of the turbulent laryngeal jet and its effect on airflow in the human intra-thoracic airways. Respir. Physiol. Neurobiol. 157, 295–309.

McDonough, J.E., Yuan, R., Suzuki, M., Seyednejad, N., Elliott, W.M., Sanchez, P.G., Wright, A.C., Gefter, W.B., Litzky, L., Coxson, H.O., 2011. Small-airway obstruction and emphysema in chronic obstructive pulmonary disease. N. Engl. J. Med. 365, 1567–1575.

Menter, F.R., 1994. Two-equation eddy-viscosity turbulence models for engineering applications. AIAA Stud. J. 32, 1598–1605.

Neff, C., Trapuzzano, M., Crane, N.B., 2018. Impact of vapor polishing on surface quality and mechanical properties of extruded ABS. Rapid Prototyp. J. 24, 501–508.

Qi, S., Zhang, B., Yue, Y., Shen, J., Teng, Y., Qian, W., Wu, J., 2018. Airflow in tracheobronchial tree of subjects with tracheal bronchus simulated using CT image based models and CFD method. J. Med. Syst. 42, 65.

Ruppel, G.L., Enright, P.L., 2012. Pulmonary function testing. Respir. Care 57, 165–175.

Sul, B., Oppito, Z., Jayasekera, S., Vanger, B., Zeller, A., Morris, M., Ruppert, K., Altes, T., Rakesh, V., Day, S., Robinson, R., Reifman, J., Wallqvist, A., 2018. Assessing airflow sensitivity to healthy and diseased lung conditions in a computational fluid dynamics model validated in vitro. J. Biomech. Eng. 140, 051009.

Sul, B., Wallqvist, A., Morris, M.J., Reifman, J., Rakesh, V., 2014. A computational study of the respiratory airflow characteristics in normal and obstructed human airways. Comput. Biol. Med. 52, 130–143.

Turato, G., Zuin, R., Saetta, M., 2001. Pathogenesis and pathology of COPD. Respiration 68, 117–128.

Tzeng, Y.-S., Lutchen, K., Albert, M., 2009. The difference in ventilation heterogeneity between asthmatic and healthy subjects quantified using hyperpolarized 3He MRI. J. Appl. Physiol. 106, 813–822.

Van den Berge, M., ten Hacken, N.H., Cohen, J., Douma, W.R., Postma, D.S., 2011. Small airway disease in asthma and COPD: clinical implications. Chest 139, 412–423.

Walker, C., Gupta, S., Hartley, R., Brightling, C.E., 2012. Computerized tomography scans in severe asthma: utility and clinical implications. Curr. Opin. Pulm. Med. 18, 42–47.

Weibel, E.R., Cournand, A.F., Richards, D.W., 1963. Morphometry of the Human Lung. Springer.

Westerweel, J., Scarano, F., 2005. Universal outlier detection for PIV data. Exp. Fluids 39, 1096–1100.

Wieneke, B., 2005. Stereo-PIV using self-calibration on particle images. Exp. Fluids 39, 267–280.

Xi, J., Longest, P.W., Martonen, T.B., 2008. Effects of the laryngeal jet on nano-and microparticle transport and deposition in an approximate model of the upper tracheobronchial airways. J. Appl. Physiol. 104, 1761–1777.

Xi, J., Si, X.A., Kim, J., Mckee, E., Lin, E.-B., 2014. Exhaled aerosol pattern discloses lung structural abnormality: a sensitivity study using computational modeling and fractal analysis. PLoS One 9, e104682.

Yang, X., Liu, Y., Luo, H., 2006. Respiratory flow in obstructed airways. J. Biomech. 39, 2743–2751.

Yin, Y., Choi, J., Hoffman, E.A., Tawhai, M.H., Lin, C.-L., 2010. Simulation of pulmonary air flow with a subject-specific boundary condition. J. Biomech. 43, 2159–2163.

Zhang, Z., Kleinstreuer, C., 2004. Airflow structures and nano-particle deposition in a human upper airway model. J. Comput. Phys. 198, 178–210.